Sensors and Materials, Vol. 38, No. 10 (2026) 6195–6204
MYU Tokyo

S & M 4675

Comparative Study of the Microstructure and Thermoelectric Properties of ZnSb Prepared via Different Synthesis Processes and Evaluated in Thermoelectric Modules

Kun-Chi Hsiao, Guan-Yu Chen, and Shih-Chen Shi*

Department of Mechanical Engineering, National Cheng Kung University (NCKU),
No. 1, University Road, Tainan 70101, Taiwan

(Received March 26, 2026; accepted July 23, 2026)

Keywords: thermoelectric materials, thermoelectric modules, process optimization

In this study, we investigate the effects of fabrication processes on the microstructure and thermoelectric performance of ZnSb mid-temperature thermoelectric materials. Among the examined routes, mechanical alloying combined with spark plasma sintering produces ZnSb with an ultrafine average grain size of ~10.7 nm, a markedly high relative density of >99%, and lower thermal conductivity, achieving a maximum figure of merit of approximately 1.0 at 600 K. In contrast, melting-based processes suffer from Zn volatilization and grain coarsening. Module testing and energy analysis further demonstrate that the optimized process enables practical thermoelectric performance, achieving a power density of 19.0 mW/cm^2, with reduced energy consumption and carbon emissions.

1. Introduction

As global energy demand grows, recovering waste heat using thermoelectric materials, which convert temperature gradients into electricity via the Seebeck effect, has become a vital solution.[1] With the thermoelectric market projected to reach $1.19 billion by 2030, its application potential in high-tech fields is immense.[2] However, overcoming low conversion efficiencies and high manufacturing costs remains essential for widespread commercialization.[3,4] This drives the ongoing search for novel materials exhibiting high electrical conductivity and low thermal conductivity.

Among mid-temperature thermoelectric materials, ZnSb is highly promising owing to its low cost and eco-friendliness.[5–7] However, traditional high-temperature melting causes Zn volatilization and coarse grain formation while methods such as rapid solidification suffer from high defect rates. Combining mechanical alloying (MA) with spark plasma sintering (SPS) effectively addresses these issues. MA prevents Zn loss and refines grains to reduce lattice thermal conductivity, while SPS minimizes porosity and significantly boosts the figure of merit

*Corresponding author: e-mail: scshi@mail.ncku.edu.tw
https://doi.org/10.18494/SAM6351

ISSN 0914-4935 © MYU K.K.
https://myukk.org/

(*ZT*).[8,9] For practical applications, the π-type thermoelectric generator remains the mainstream architecture because of its simplicity and high efficiency. Nevertheless, modules often face interfacial stability challenges, including thermal expansion mismatch and elemental diffusion that form brittle intermetallic compounds.[10] Incorporating diffusion barriers, buffer layers, or low-melting-point solders is therefore essential to extend module lifespans.

Despite these advancements, a clear research gap remains. A systematic comparative study elucidating exactly how different synthesis sequences affect both the microstructural evolution and the final practical module-level performance is currently lacking. To address the Zn volatilization and high thermal conductivity issues in traditional ZnSb synthesis[11,12] and to bridge this gap, we hypothesize that combining MA with SPS to bypass high-temperature melting can effectively suppress grain coarsening, and a highly dense, uniform nanocrystalline architecture can be constructed. This microstructure is expected to significantly enhance phonon scattering, reducing lattice thermal conductivity and markedly improving the thermoelectric *ZT*. To verify this, we systematically compare three ZnSb processing routes. Finally, a π-type thermoelectric module is fabricated using the optimized ZnSb to evaluate its power generation performance and process economy, demonstrating its practical viability for mid-temperature waste heat recovery.

2. Materials and Methods

2.1 Materials

The commercial reagents used in this study include nickel nitrate (97%, Katayama Chemical, Japan), ferric nitrate (98%, Daejung, Japan), urea (Katayama Chemical, Japan), ammonium fluoride (97%, NH_4F, Showa, Japan), tetraethylenepentamine (TEPA, Thermo Scientific, USA), ethanol (95%, Shin-Shin Chemical Co., Taiwan), CO_2 gas (99.99%, Yun Hai Gas, Taiwan), nickel foam (Shin-Shin Chemical Co., Taiwan), and 304 stainless steel (Xin Rui Fa Metal Co., Ltd., Taiwan). Zinc (Zn) and antimony (Sb) precursors were utilized as the primary raw materials for the synthesis of the thermoelectric alloys.

2.2 Synthesis of ZnSb bulk

To systematically investigate the effect of processing routes on the material properties, three different synthesis methods (designated as Processes A, B, and C) were designed. First, high-purity Zn and Sb powders were weighed to a strict stoichiometric molar ratio of 1:1. For the mechanical milling steps, the powders were placed in stainless-steel vials with stainless-steel balls and milled at a rotational speed of 550 rpm for 6 h in an inert argon atmosphere to prevent oxidation. For the melting steps (Processes A and B), the materials were heated in crucibles in an argon atmosphere to specific temperatures (600, 650, or 700 °C) and held for 3 h to promote alloy formation. The detailed experimental parameters, including ball milling, high-temperature melting, and consolidation, are summarized in Table 1. Notably, Process C utilizes intense mechanical collisions during the high-energy ball milling step to drive the alloying reaction, entirely bypassing the conventional high-temperature melting step required in Processes A and B. Following the respective synthesis routes, all powders were ultimately consolidated by SPS.

Table 1
Detailed experimental parameters for the synthesis of ZnSb bulks via Processes A, B, and C.

Process	Pre-milling	Melting (Inert atm.)	Post-milling	Sintering (SPS)
A	—	600, 650, 700 °C (3 h)	550 rpm (6 h)	450 °C, 50 MPa, 10 min
B	550 rpm (6 h)	600, 650, 700 °C (3 h)	550 rpm (6 h)	450 °C, 50 MPa, 10 min
C	550 rpm (6 h)	—	—	450 °C, 50 MPa, 10 min

The SPS process was conducted in a vacuum environment at a constant sintering temperature of 450 °C under a uniaxial pressure of 50 MPa with a holding time of 10 min.

2.3 Material characterization and thermoelectric measurements

The crystal phase compositions of the samples were identified by X-ray diffraction (XRD) using Cu Kα radiation with a scanning range of 2θ = 20–60°. The microstructures and grain sizes were examined by scanning electron microscopy (SEM) and transmission electron microscopy (TEM). The crystal structure and lattice spacing were further analyzed via selected-area electron diffraction (SAED) and high-resolution TEM (HRTEM). The relative densities of the sintered bulks were determined by the Archimedes method.

For thermoelectric properties, the electrical conductivity and Seebeck coefficient were measured simultaneously using a ZEM-3 system over a temperature range of 300–700 K. The thermal conductivity was calculated from the material's density, specific heat, and thermal diffusivity, where the thermal diffusivity was measured using a physical property measurement system (PPMS). The dimensionless thermoelectric *ZT* was then calculated using these obtained parameters.

2.4 Thermoelectric module fabrication and evaluation

To evaluate the practical power generation capability, a π-type thermoelectric module was assembled. In this system, the optimized p-type ZnSb prepared in this study (for hole transport) and the n-type AgSe material developed in our laboratory (for electron transport) served as the active thermoelectric legs to convert the temperature gradient into electrical energy. These legs were bonded to copper electrodes, which act as electrical interconnects to connect the p-n legs in series. Furthermore, the assembly was sandwiched between ceramic substrates, which provide essential mechanical support, electrical insulation, and effective thermal conduction. Finally, soldering was utilized not only for mechanical bonding but also to minimize the interfacial electrical and thermal contact resistance between the thermoelectric legs and the electrodes.

3. Results and Discussion

3.1 XRD phase analysis of ZnSb under different melting conditions

Figure 1 presents the XRD patterns of samples synthesized via Process A [Figs. 1(a)–1(c)] and Process B [Figs. 1(d)–1(f)] at various melting temperatures (600, 650, and 700 °C). The results indicate that the primary diffraction peaks of all samples agree perfectly with the orthorhombic ZnSb phase (space group Pbca), confirming that both processes successfully form a ZnSb-dominated alloy phase.

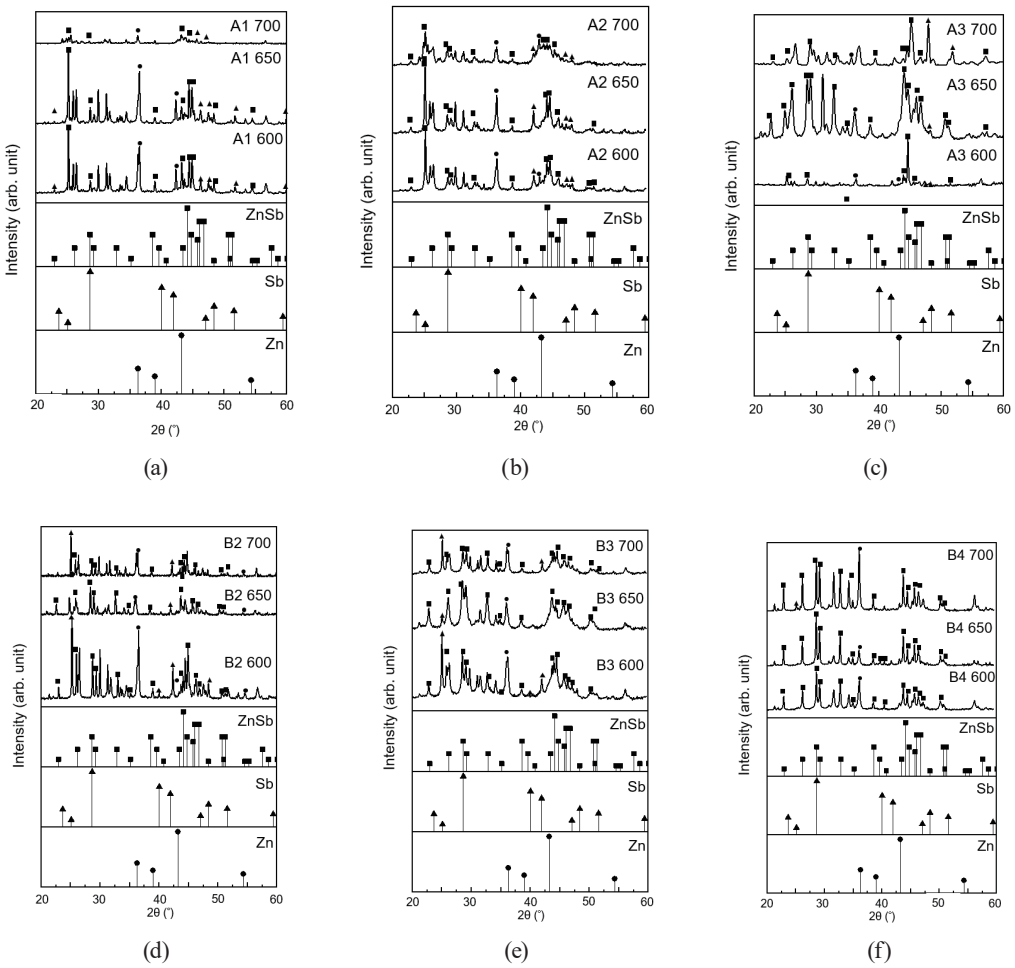


Fig. 1. XRD patterns of ZnSb samples synthesized at various melting temperatures (600, 650, and 700 ℃) via Process (a) A1, (b) A2, (c) A3, and Process (d) B2, (e) B3, (f) B4.

For Process A, the characteristic peaks of ZnSb are clearly visible at 600 ℃ (A3 600); however, minor residual peaks corresponding to metallic Zn and Sb are still observed, indicating incomplete alloying. When the melting temperature is increased to 650 ℃ (A3 650), the intensity of the ZnSb diffraction peaks significantly improves, but that of the residual Zn/Sb peaks markedly decreases. This suggests that higher temperatures facilitate elemental diffusion and phase formation, resulting in a more complete ZnSb phase with enhanced crystallinity. Conversely, further elevating the temperature to 700 ℃ (A3 700) leads to peak broadening and decreased intensity, accompanied by the reappearance of Zn secondary phase peaks. This phenomenon is presumably attributed to Zn volatilization and lattice disordering at excessive temperatures, highlighting that overly high melting temperatures are detrimental to phase stability and crystalline quality.

Process B exhibits a similar phase evolution trend. At 600 ℃ (B4 600), the alloying reaction remains incomplete, with notable residual diffraction peaks. At 650 ℃ (B4 650), the combination of double-milling and an appropriate high melting temperature effectively promotes elemental diffusion and complete reaction, leading to substantially intensified ZnSb main peaks and weakened residual peaks, thereby achieving optimal phase purity. When the temperature is

further increased to 700 °C (B4 700), ZnSb remains the primary phase; nevertheless, some diffraction peaks exhibit broadening and uneven intensity. This degradation in crystalline quality relative to that under the 650 °C condition is likely associated with rapid grain growth, internal strain accumulation, or local Zn volatilization at elevated temperatures.

In conclusion, the melting temperature plays a critical role in the phase formation and crystallinity of ZnSb in both processes, necessitating strict parameter optimization. For both routes, 650 °C emerges as the most suitable condition to balance compl*ete al*loying with superior crystalline quality.

3.2 Relative density and porosity of ZnSb bulk

Table 2 summarizes the relative densities and porosities of the ZnSb bulk materials prepared via Processes A, B, and C, measured by the Archimedes method following SPS. The results indicate that the processing route and melting temperature significantly affect the densification behavior of the ZnSb bulks.

For the Process A samples, the relative densities range from 92.74 to 94.65%, corresponding to porosities of 5.35–7.26%. The slightly higher porosity observed in the A3 650 sample is presumably attributed to rapid grain growth under mid-to-high temperature conditions, which restricts particle rearrangement during sintering. Overall, Process A provides adequate compaction, yet its densification degree remains notably sensitive to the processing temperature.

Process B samples exhibit a broader relative density range (89.48–95.80%) and a corresponding porosity variation (4.20–10.52%), indicating lower compaction stability. This phenomenon likely stems from uneven particle size distribution or localized agglomeration caused by the double-milling steps before and after melting, which hinders the complete elimination of pores during sintering. Although the B4 650 sample achieves a higher relative density, Process B generally tends to produce structures with higher porosity.

In contrast, the Process C sample demonstrates the most outstanding densification performance, achieving a markedly high relative density of 99.07% and a mere 0.92% porosity, significantly outperforming both Process A and B samples. This indicates that direct SPS application following MA effectively enhances powder uniformity and promotes tight inter-particle bonding, thereby profoundly suppressing pore formation.

Table 2
Measured relative densities and porosities of ZnSb bulk materials synthesized via different processes.

Process	Temperature (°C)	W_a (g) (in air)	W_l (g) (in water)	Water denstity (g/cm^3)	ρ (g/cm^3)	Relative density / standard: 6.39 g/cm^3	Porosity
A	600	3.03	2.53	0.9968	6.33	94.55	5.45
	650	9.04	7.52	0.9968	6.33	92.74	7.26
	700	6.97	5.82	0.9968	6.33	94.65	5.35
B	600	4.27	3.59	0.9968	6.33	90.26	9.47
	650	5.80	4.86	0.9968	6.33	95.80	4.20
	700	4.28	3.53	0.9968	6.33	89.48	10.52
C	—	5.11	4.28	0.9968	6.33	99.07	0.92

3.3 Grain size and TEM analysis of ZnSb

Table 3 summarizes the average grain sizes and standard deviations of the ZnSb bulk samples prepared under various processing conditions, clearly indicating that the processing route and melting temperature significantly affect grain growth behavior. For Process A, the sample melted at 600 °C (A3 600) exhibits a relatively fine and uniform grain structure with an average grain size of approximately 65.2 nm. However, as the melting temperature increases to 650 and 700 °C, the grain size increases significantly to 154.1 and 122.9 nm, respectively, accompanied by a notable increase in standard deviation. This suggests that high-temperature melting and slow cooling conditions readily lead to excessive grain growth and a nonuniform size distribution.

The Process B samples exhibit a similar trend; nevertheless, their overall grain sizes are larger than those of the Process A samples, and the size distribution is more scattered. The average grain size of B4-600 is 99.4 nm, which further grew to 154.5 and 139.7 nm at 650 and 700 °C, respectively, with corresponding standard deviations exceeding ±100 nm. This indicates that under the combined effects of multiple milling steps and high-temperature melting, grain growth behavior is difficult to control effectively, making the material prone to forming a nonuniform microstructure.

In stark contrast, Process C sample C2 demonstrates distinct grain characteristics, achieving an average grain size of only ~10.7 nm with a standard deviation of merely ±2.3 nm, which reveals an exceptionally fine and highly uniform grain distribution. This favorable result is attributed to Process C employing MA followed directly by SPS, thereby avoiding the rapid grain growth typically observed during high-temperature melting and effectively suppressing grain coarsening.

Figures 2(a)–2(c) present the SAED patterns and HRTEM images of the ZnSb samples prepared via the different processes. The SAED patterns for the samples from Processes A and B display clear diffraction spots, indicating good retained crystallinity. However, variations in crystal orientation and local lattice spacing differences are observable at different temperatures, reflecting the strain and defect recombination induced by the high-temperature treatments. Conversely, the SAED pattern of the Process C sample exhibits a highly regular and symmetric diffraction dot array. Furthermore, the HRTEM image clearly resolves the lattice fringes with a measured d-spacing of approximately 0.409 nm, demonstrating an intact and stable crystal structure.

Combining the grain size statistics with the TEM observations, it is evident that Process C effectively achieves a fine and uniform nanocrystalline structure. This architecture significantly

Table 3
Average grain sizes and standard deviations of ZnSb samples prepared under different processing conditions.

Process	Average grain size (nm)	Standard deviation (nm)
A3 600	65.2	±39.0
A3 650	154.1	±109.2
A3 700	122.9	±72.3
B4 600	99.4	±138.8
B4 650	154.5	±168.0
B4 700	139.7	±116.4
C2	10.7	±2.3

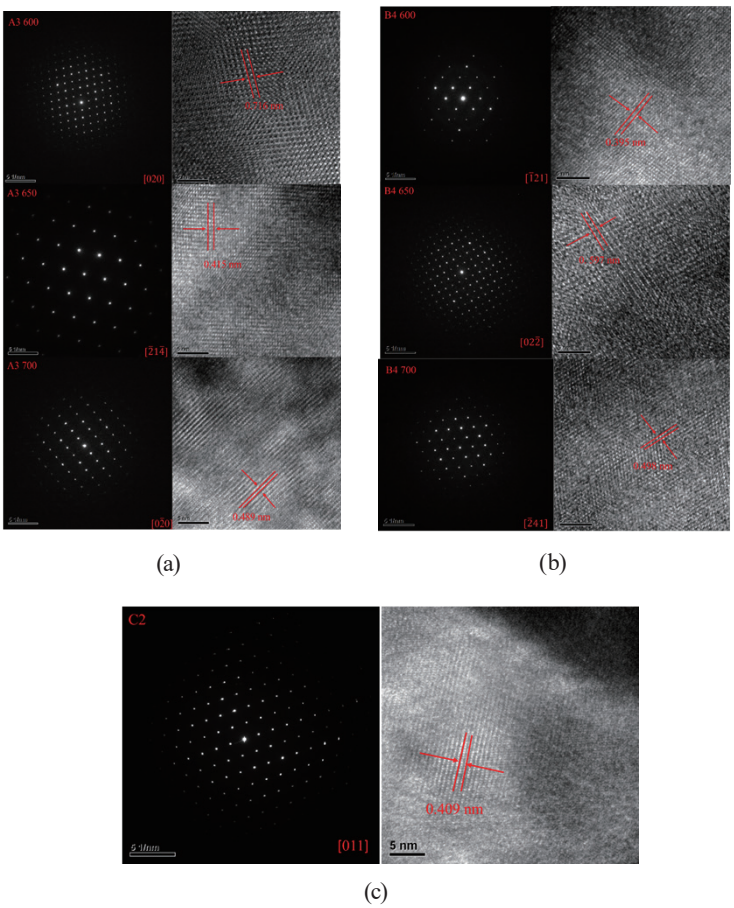


Fig. 2. (Color online) Microstructures of ZnSb bulk samples: SAED and HRTEM images for (a) Process A, (b) Process B, and (c) Process C.

increases the grain boundary density to enhance phonon scattering, establishing a robust microstructural foundation for reducing thermal conductivity and improving the overall thermoelectric performance. By comparison, Processes A and B are far more susceptible to grain coarsening and uneven size distributions under high-temperature melting conditions, indicating a relative lack of microstructural stability.

3.4 Thermoelectric properties and module performance

Figure 3 illustrates the temperature-dependent thermoelectric properties of the ZnSb bulk samples synthesized by different processes over the range of 300–700 K. First, regarding electrical conductivity (σ) [Fig. 3(a)], the samples from Processes A and B exhibit relatively high electrical conductivity in the low-temperature region, which gradually decreases or stabilizes as the temperature increases. Fundamentally, in heavily doped semiconductors such as ZnSb, electrical conductivity is governed by the competition between carrier concentration and carrier mobility. As temperature increases, acoustic phonon scattering intensifies, significantly reducing carrier mobility and thus lowering the conductivity. In contrast, the Process C sample maintains a relatively high and stable electrical conductivity throughout the entire temperature range. This stability implies that its highly dense, defect-free nanocrystalline structure [Fig. 3(c)], achieved by avoiding high-temperature melting, successfully prevents Zn volatilization.

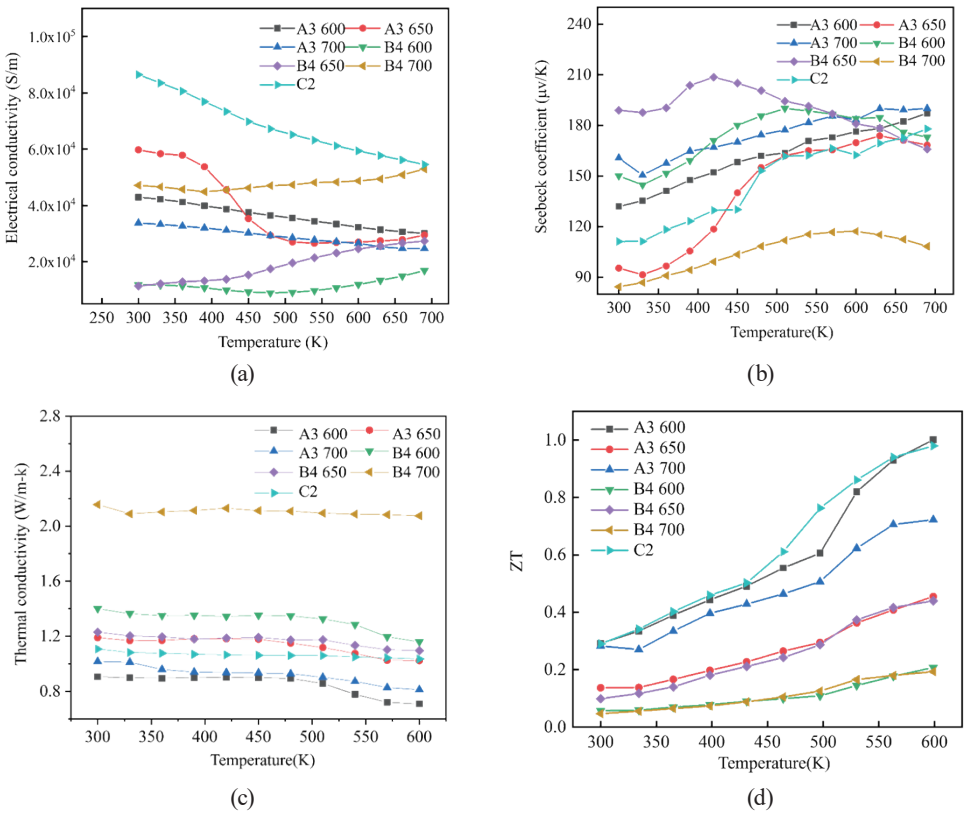


Fig. 3. (Color online) Thermoelectric properties of the prepared ZnSb samples as a function of temperature: (a) electrical conductivity, (b) Seebeck coefficient, (c) thermal conductivity, and (d) ZT.

This preserves a stable majority hole concentration that effectively compensates for the mobility degradation at elevated temperatures. The Seebeck coefficient (S) results in Fig. 3(b) show positive values for all samples, confirming their p-type thermoelectric nature. For Processes A and B, the Seebeck coefficient levels off or decreases in the high-temperature region (>500 K). This phenomenon is a classic manifestation of the bipolar effect, where intrinsic thermal excitation generates minority carriers (electrons) that negatively offset the thermopower contributed by the majority holes. This effect is often exacerbated by Zn vacancies and structural defects induced during high-temperature melting. Conversely, the Process C sample displays a steady increasing trend without obvious bipolar roll-off. This deeper structural integrity demonstrates that the MA+SPS process maintains the stability of the band structure and effectively suppresses the premature activation of minority carriers, thereby sustaining a high Seebeck coefficient up to 700 K.

In terms of thermal conductivity (κ) [Fig. 3(c)], the Process C sample consistently exhibits the lowest and most stable thermal conductivity across all temperature ranges, further confirming that its pure nanocrystalline structure can effectively enhance phonon scattering. The thermal conductivity of the Process A samples is the second lowest, whereas the Process B samples generally show higher thermal conductivity because of their larger and unevenly distributed grains. The dimensionless thermoelectric ZT calculated from the above parameters [Fig. 3(d)] reveals that the ZT values of all samples increase with temperature. Notably, owing to its combination of stable electrical properties, a relatively high Seebeck coefficient, and the lowest

thermal conductivity, the *ZT* value of the Process C sample increases rapidly, reaching an outstanding value of approximately 1.0 at around 600 K, thereby demonstrating the optimal thermoelectric performance. The significant enhancement in the thermoelectric performance of the Process C samples can be attributed to two main physical mechanisms. First, the enhanced phonon scattering at the dense grain boundaries of the uniform nanocrystalline structure (~10.7 nm) effectively impedes heat transfer, leading to a markedly reduced lattice thermal conductivity. Second, by bypassing the conventional high-temperature melting step, MA suppresses Zn volatilization and detrimental defect formation (e.g., Zn vacancies and unreacted secondary phases). This preserves the stoichiometric integrity and phase purity of the ZnSb lattice. Combined with the ultrahigh relative density (>99%) achieved via rapid SPS consolidation, this optimized microstructure allows for a decoupling of electrical and thermal transport, maintaining stable carrier mobility while severely restricting phonon propagation, thereby maximizing the *ZT* value.

3.5 Benchmark comparison and practical application evaluation

Referring to the superior material properties described above, in this study, we further assembled the synthesized p-type ZnSb and an n-type AgSe into a thermoelectric power generation module to evaluate its practical application potential. To benchmark the module's performance, its measured power density was compared directly with those reported in existing literature. Previous studies on related mid-temperature thermoelectric modules have revealed power densities ranging from approximately 9.2 to 23.0 mW/cm^2[13–15]. In comparison, the ZnSb/AgSe thermoelectric module fabricated in this study achieves a marked power density of 19.0 mW/cm^2. This overall performance is highly comparable to those obtained in most state-of-the-art research, demonstrating its excellent energy conversion capability.

Notably, although we adopted a significantly simplified and low-energy-consumption processing route (Process C) for material preparation, the module still achieves highly competitive output performance. This clearly indicates that the proposed synthesis process offers a distinct advantage in balancing thermoelectric efficiency with manufacturing economy. These results fully demonstrate that the optimized ZnSb thermoelectric material and the corresponding module design have enormous potential for practical applications in mid-temperature waste heat recovery systems.

4. Conclusions

We demonstrated that MA followed by SPS (Process C) is the optimal preparation route for ZnSb thermoelectric materials. This approach effectively prevents high-temperature grain coarsening, yielding a pure, highly dense (>99%) nanocrystalline structure with an average grain size of ~10.7 nm. This fine-grained architecture significantly suppresses lattice thermal conductivity while maintaining electrical conductivity, resulting in a stable and enhanced thermoelectric *ZT*.

The key contribution of this work is the demonstration that a streamlined, melting-free solid-state route can successfully decouple electrical and thermal transports, effectively breaking the traditional trade-off between achieving high thermoelectric performance and maintaining low

manufacturing costs. Moreover, Process C offers marked economic and environmental advantages over traditional melting techniques by markedly reducing processing time, energy consumption, and carbon footprints. When integrated into a ZnSb/AgSe thermoelectric module, the material exhibited excellent power generation performance (19.0 mW/cm^2). Ultimately, the broader impact of this study lies in establishing a highly energy-efficient and low-carbon manufacturing paradigm. The findings of this research bridge the gap between laboratory-scale material synthesis and practical device application, significantly accelerating the commercial viability of mid-temperature thermoelectric modules for industrial waste heat recovery and contributing to global energy sustainability.

Acknowledgments

This work was supported by the National Science and Technology Council (NSTC), Taiwan, under Grants No. 112-2221-E-006-173, 113-2221-E-006-087-MY2, 113-2221-E-006-112-MY2, and 113-2221-E-006-116. The authors gratefully acknowledge the Core Facility Center at National Cheng Kung University, Taiwan, for providing access to the EM000800 and SQUID000200 instruments, which were funded by the NSTC project 114-2740-M-006-001. Additional support from the Higher Education Sprout Project of the Ministry of Education, Taiwan, through the Headquarters of University Advancement at National Cheng Kung University (NCKU), is also gratefully acknowledged.

References

1 H. Jouhara, A. Żabnieńska-Góra, N. Khordehgah, Q. Doraghi, L. Ahmad, L. Norman, B. Axcell, L. Wrobel, and S. Dai: Int. J. Thermofluids **9** (2021) 100063. https://doi.org/10.1016/j.ijft.2021.100063
2 P. Baskaran and M. Rajasekar: RSC Adv. **14** (2024) 21706. https://doi.org/10.1039/D4RA03625E
3 W. Li, B. Poudel, R. A. Kishore, A. Nozariasbmarz, N. Liu, Y. Zhang, and S. Priya: Adv. Mater. **35** (2023) 2210407. https://doi.org/10.1002/adma.202210407
4 B. Jiang, X. Liu, Q. Wang, J. Cui, B. Jia, Y. Zhu, J. Feng, Y. Qiu, M. Gu, and Z. Ge: Energy Environ. Sci. **13** (2020) 579. https://doi.org/10.1039/C9EE03410B
5 R. Biswas, S. Mukherjee, R. Mallik, S. Vitta, and T. Dasgupta: Mater. Today Energy **12** (2019) 107. https://doi.org/10.1016/j.mtener.2018.12.014
6 Y.-H. Chu, Z.-Q. Huang, Z.-R. Yang, F.-H. Lin, K.-C. Chang, R. Suriakarthick, and C.-J. Liu: J. Eur. Ceram. Soc. **39** (2019) 4177. https://doi.org/10.1016/j.jeurceramsoc.2019.06.033
7 V. C. Theja, V. Karthikeyan, S. Nayak, K. U. Kandira, D. S. Assi, V. Kannan, and V. A. Roy: J. Phys. Chem. Solids **178** (2023) 111329. https://doi.org/10.1016/j.jpcs.2023.111329
8 P.-Y. Lee and P.-H. Lin: Energies **11** (2018) 1200. https://doi.org/10.3390/en11051200
9 M. K. Keshavarz, C.-W. T. Lo, S. Turenne, Y. Mozharivskyj, and N. J. Quitoriano: J. Manuf. Mater. Process. **3** (2019) 58. https://doi.org/10.3390/jmmp3030058
10 S. Liu, L. Ma, C. Zhen, D. Li, Y. Wang, Q. Jia, and F. Guo: Mater. Charact. **206** (2023) 113384. https://doi.org/10.1016/j.matchar.2023.113384
11 X. Song, M. Schrade, N. Masó, and T. G. Finstad: J. Alloys Compd. **710** (2017) 762. https://doi.org/10.1016/j.jallcom.2017.03.339
12 R. Biswas, S. Vitta, and T. Dasgupta: Mater. Res. Bull. **149** (2022) 111702. https://doi.org/10.1016/j.materresbull.2021.111702
13 N. Van Toan, T. T. K. Tuoi, N. Van Hieu, and T. Ono: Energy Convers. Manage. **245** (2021) 114571. https://doi.org/10.1016/j.enconman.2021.114571
14 N. Van Toan, T. T. K. Tuoi, N. H. Trung, K. F. Samat, N. Van Hieu, and T. Ono: Latest Research on Energy Recovery, P. Vizureanu, Ed. (IntechOpen, London, 2022) Chap. 2. https://doi.org/10.5772/intechopen.102649
15 N. Kanas, M. Bittner, T. D. Desissa, S. P. Singh, T. Norby, A. Feldhoff, T. Grande, K. Wiik, and M.-A. Einarsrud: ACS Omega **3** (2018) 9899. https://doi.org/10.1021/acsomega.8b01357